RSC Advances

PAPER

View Article Online
View Journal | View Issue

Cite this: *RSC Adv.*, 2021, **11**, 19630

Heterostructure Ni_3S_4–MoS_2 with interfacial electron redistribution used for enhancing hydrogen evolution†

Jingmin Ge,[a] Jiaxing Jin,[a] Yanming Cao,[a] Meihong Jiang,[a] Fazhi Zhang,[a] Hongling Guo*[b] and Xiaodong Lei*[a]

Developing highly effective and inexpensive electrocatalysts for hydrogen evolution reaction (HER), particularly in a water-alkaline electrolyzer, are crucial to large-scale industrialization. The earth-abundant molybdenum disulfide (MoS_2) is an ideal electrocatalyst in acidic media but suffers from a high overpotential in alkaline solution. Herein, nanospherical heterostructure Ni_3S_4–MoS_2 was obtained *via* a one-pot synthesis method, in which Ni_3S_4 was uniformly integrated with MoS_2 ultrathin nanosheets. There were abundant heterojunctions in the as-synthesized catalyst, which were verified by X-ray photoelectron spectroscopy (XPS) and high-resolution transmission electron microscopy (HRTEM). The structure features with interfacial electron redistribution was proved by XPS and density functional theory (DFT) calculations, which offered several advantages to promote the HER activity of MoS_2, including increased specific surface area, exposed abundant active edge sites and improved electron transfer. Ni_3S_4–MoS_2 exhibited a low overpotential of 116 mV at 10 mA cm^{-2} in an alkaline solution with a corresponding Tafel slope of 81 mV dec^{-1} and long-term stability of over 20 h. DFT simulations indicated that the synergistic effects in the system with the chemisorption of H on the (002) plane of MoS_2 and OH on the (311) plane of Ni_3S_4 accelerated the rate-determining water dissociation steps of HER. This study provides a valuable route for the design and synthesis of inexpensive and efficient HER electrocatalyst, heterostructure Ni_3S_4–MoS_2.

Received 12th April 2021
Accepted 17th May 2021

DOI: 10.1039/d1ra02828f

rsc.li/rsc-advances

Introduction

With the increasing environmental protection demands, developing sustainable and fossil-free renewable energy plays a major role.[1] Due to its environmentally friendly, zero-emission, high-energy capacity and sustainable merits, hydrogen (H_2) has received extensive attention.[2] The most efficient method to generate H_2 ($2H_2O \rightarrow 2H_2 + O_2$) is water splitting by electric power generated from renewable energy sources.[3–5] Currently, some noble metals, such as Pt, Rh and Ir, have been proved to possess excellent catalytic performance as HER electrocatalysts, including low overpotential, low Tafel slope and low impedance.[6,7] However, the exorbitant cost and limited earth abundance of these noble metal materials have hindered their industrialization and commercialization.[8] Therefore, developing electrocatalysts that are low cost, highly active and stable from nonprecious and earth-abundant metal materials is urgent.

In recent years, earth-abundant 2D MoS_2 has been considered as an ideal alternative to the precious Pt-based catalysts as the next-generation electrocatalytic material due to its unique structure and chemical properties.[9–11] DFT calculations indicated that MoS_2 exhibits excellent HER performance in acidic solutions since its edge sites permit a near-optimal hydrogen adsorption free energy ($\Delta G_{H^*} = 0.08$ eV).[12] Moreover, the tremendous amount of S sites in the basal plane of pure MoS_2 are quite inert and not sufficiently utilized.[13] Unfortunately, MoS_2 has also been found to have poor activity in alkaline media,[14] even though alkaline catalysis is a more widespread application. Numerous strategies have been employed to improve the catalytic activity of 2D MoS_2, such as generating the sulfur vacancies,[15] introducing heteroatoms,[16] changing conductive supports.[17] It has been both experimentally and theoretically identified that the fabrication of heterogeneous nanostructures with abundant and accessible exposed active sites is a very effective way for improving the catalytic activity.[18]

MoS_2 decorated with transition metals, such as Fe, Co and Ni, by heterostructure engineering has shown excellent electrocatalytic performance.[19] Because of the versatile electronic structure of these metals and the ability to fill d orbitals with

[a]State Key Laboratory of Chemical Resource Engineering, Beijing University of Chemical Technology, Beijing, 100029, China. E-mail: leixd@mail.buct.edu.cn; Fax: +86-10-64455357

[b]Institute of Forensic Science, Ministry of Public Security, Beijing, 100038, China. E-mail: guohongling1234@163.com

† Electronic supplementary information (ESI) available. See DOI: 10.1039/d1ra02828f

electrons from another transition metal, they provide distinctive catalytic properties. For example, nickel-based catalysts have been shown to have impressive potential for HER electrocatalysts due to their conductivity and low cost.[20,21] Some reports have indicated that constructing heterostructure for MoS_2 *via* introducing nickel sulfides (*e.g.*, Ni_3S_2,[22] NiS_2 (ref. 23) and NiS[24]) could provide superior HER activity. However, the intrinsic motivation of the enhanced catalytic performance is not clear. Moreover, the impact of constructing a heterogeneous structure *via* introducing Ni_3S_4 into MoS_2 on HER performance remains to be studied. Moreover, an in-depth understanding of the interfacial electron redistribution for the improved HER performance is important for its wide application.

In this study, we fabricated the heterostructure Ni_3S_4–MoS_2 with a nanospherical morphology *via* a one-step hydrothermal strategy and applied it as an HER catalyst. To improve the electronic conductivity and expose abundant active edge sites of MoS_2, we constructed the heterostructure *via* introducing Ni_3S_4 into MoS_2 ultra-thin nanosheets, which significantly enhanced the HER activity. The heterostructure of Ni_3S_4–MoS_2 was investigated *via* XPS, SEM and HRTEM techniques. For researching the electron redistribution on the interface of Ni_3S_4–MoS_2 and the mechanism of electro-catalysis during HER, we also applied the DFT simulation. It is indicated that the heterostructure Ni_3S_4–MoS_2 optimized water dissociation energies and H* absorption free energy.

Experimental section

Materials

Sodium molybdate (VI) dihydrate ($Na_2MoO_4 \cdot 2H_2O$), nickel(II) chloride hexahydrate ($NiCl_2 \cdot 6H_2O$), urea, sodium sulfide nonahydrate ($Na_2S \cdot 9H_2O$) and thiourea (CH_4N_2S) were obtained from Beijing Chemical Works. A 5 wt% Nafion solution was obtained from Du Pont China Holding Co., Ltd. A nickel foam (NF) having a thickness of 0.5 mm was bought from Changsha Lyrun New Materials Co., Ltd., and it (cut as 1.0 cm × 1.0 cm in size) was washed with hydrochloric acid, ethanol and deionized water. All other chemicals were of analytical grade and were purchased from Sinopharm Chemical Reagents Co. All chemicals were used without further purification.

Synthesis of MoS_2, Ni_4S_3–MoS_2 and Ni_4S_3 nanosheets

3.5 mmol (0.847 g) of $Na_2MoO_4 \cdot 2H_2O$ and 15 mmol (1.14 g) of thiourea were dissolved in 30 mL of deionized water and dispersed by ultrasonication for 10 min to form a uniform solution. The mixture was transferred into a 50 mL Teflon-lined stainless-steel autoclave and maintained at 180 °C for 24 h. The as-prepared MoS_2 was washed with deionized water and ethanol several times and then dried in a vacuum at 60 °C. Ni_3S_4–MoS_2 was synthesized by a simple one-pot step method that was the same as the above process for MoS_2. However, in the $Na_2MoO_4 \cdot 2H_2O$ and thiourea mixed solution, different amounts of $NiCl_2 \cdot 6H_2O$ were added. Then, the Ni_3S_4–MoS_2 nanosheets were obtained after the same hydrothermal treatment, washing and drying.

Ni_3S_4 was prepared according to the method in the reported literature.[25] Briefly, 1.5 mmol (0.357 g) of $NiCl_2 \cdot 6H_2O$ and 10 mmol (0.60 g) of urea were dissolved in 30 mL deionized water, and the mixture was dispersed by ultrasonication for 10 min to form a uniform solution. The solution was then transferred into a 50 mL Teflon-lined stainless-steel autoclave and maintained at 130 °C for 2 h. The as-prepared $Ni(OH)_2$ was washed with deionized water and ethanol several times and then dried in a vacuum at 60 °C. Then, the as-prepared $Ni(OH)_2$ precursor together with 30 mL of 15 mmol (3.6 g) sodium sulfide ($Na_2S \cdot 9H_2O$) aqueous solution was placed in the Teflon-lined stainless-steel autoclave and maintained at 90 °C for 9 h. The as-prepared Ni_3S_4 was washed with deionized water and ethanol several times and then dried in a vacuum at 60 °C for 12 h.

Characterization

X-ray diffraction (XRD) patterns were collected on a Rigaku XRD-6000 diffractometer using Cu Kα radiation from 3° to 80° at the scan rate of 10° min^{-1}. The morphologies were investigated *via* SEM (Zeiss SUPRA 55) at an accelerating voltage of 20 kV. A Brunauer–Emmett–Teller (BET, ASAP 2460) apparatus was used to measure the surface area. HRTEM images were recorded using a JEOL JEM-2010 field-emission transmission electron microscope at an accelerating voltage of 200 kV, combined with energy-dispersive X-ray spectroscopy (EDS). XPS measurements were performed on a Thermo VG ESCALAB 250 X-ray photoelectron spectrometer with Al Kα radiation at a pressure of about 2×10^{-9} Pa. Inductively coupled plasma-optical emission spectrometry (ICP-OES) was adopted to analyze the chemical components of the catalysts.

Electrochemical measurements

Electrochemical measurements were performed on an electrochemical workstation (CHI 660E, CH Instruments Inc., Chenhua, Shanghai) using a three-electrode mode in an Ar-saturated 1 mol L^{-1} KOH aqueous solution. A platinum electrode was used as the counter electrode, a sliver/sliver chloride (Ag/AgCl) electrode was used as the reference electrode, and the as-fabricated materials were used as the working electrodes. The potentials were converted to the RHE scale using the following Nernst equation: (E(RHE) = E(Ag/AgCl) + 0.059 pH + 0.197). To accelerate the electrochemical performance tests, 5 mg of the as-prepared catalysts, 2 mg conductive carbon, 35 μL of the 5 wt% Nafion solution and 1 mL anhydrous ethanol were mixed and ultrasonicated for 10 min to form homogeneous catalyst inks. The catalyst inks were dripped respectively onto the as-prepared NF to obtain the working electrodes with a loading of ~5 mg cm^{-2}, which were dried at 60 °C for 1 h. The electrochemical impedance spectroscopy (EIS) tests were performed in the frequency range from 100 kHz to 0.1 Hz at an overpotential of 180 mV. The cyclic voltammograms (CV) were obtained between 0.1 and −0.3 V *vs.* RHE at 100 mV s^{-1} to investigate the cycling stability. The long-term stability tests were recorded by taking a chronoamperometric curve current density that reached 10 mA cm^{-2}. All data were presented

without IR compensation, and all the electrochemical tests were tested at room temperature.

Computational methods

All first principles calculations were performed *via* DFT in the Cambridge Sequential Total Energy Package (CASTEP) module in the Materials Studio. The MoS_2 (002) plane consisting of six layers of Mo and S, and the Ni_3S_4 (311) slab composed of six layers of atoms were constructed as our models, because the (002) plane of MoS_2 and the (311) plane of Ni_3S_4 were dominant crystal faces from the HRTEM images. The exchange–correlation interactions were treated within the generalized gradient approximation of the Perdew–Burke–Ernzerhof (PBE) type. The plane-wave cutoff energy was 400 eV, and a k-mesh of $3 \times 3 \times 1$ was adopted to sample the Brillouin zone. The convergence threshold for energy and Hellmann–Feynman forces on each atom were set to 10^{-5} eV and 0.01 eV $Å^{-1}$. Vacuum layers of 15 Å were introduced to minimize interactions between adjacent layers in all supercells.[15] All the atom positions in the model were optimized by the conjugate-gradient optimization procedure.

Gibbs free-energy of the adsorption atomic hydrogen was calculated as the following formula:

$$\Delta G = \Delta E + \Delta ZPE - T\Delta S \quad (1)$$

where ΔE is the adsorption energy of adsorbed species on the given unit cell. ΔZPE and $T\Delta S$ are the zero-point energy and entropy difference of hydrogen in the adsorbed state and the gas phase, respectively. The value of *ZPE* and *TS* for the

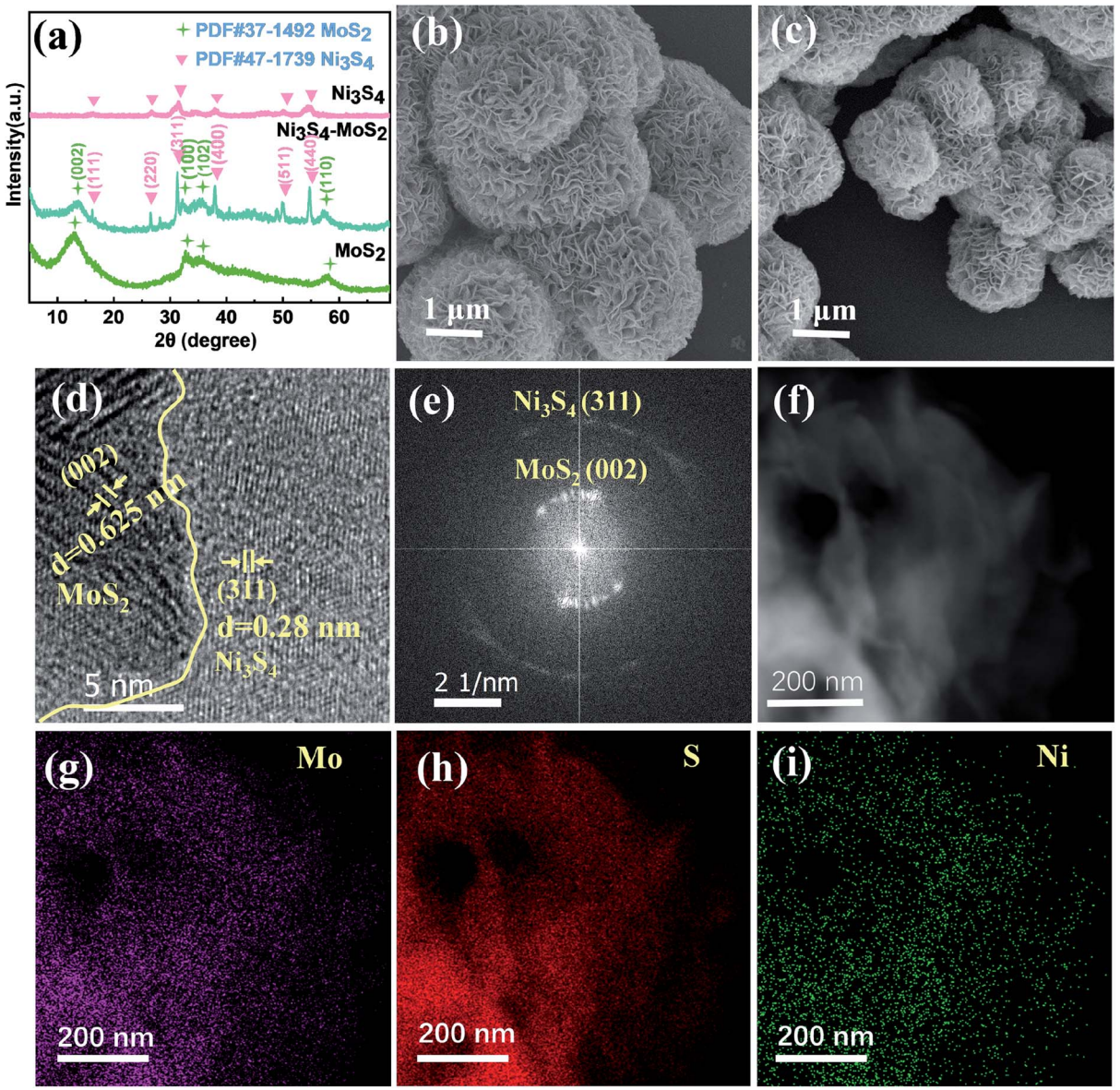

Fig. 1 (a) XRD patterns of Ni_3S_4–MoS_2, Ni_3S_4 and MoS_2. (b) SEM image of the Ni_3S_4–MoS_2. (c) SEM image of the MoS_2. (d) TEM image and (e) corresponding SAED pattern of Ni_3S_4–MoS_2. (f) TEM image of Ni_3S_4–MoS_2 and corresponding elemental mappings: Mo (g), S (h) and Ni (i).

adsorbed species were calculated from the vibration frequencies, as shown in the previous literature.[15]

Results and discussion

Morphology and structure of Ni_3S_4–MoS_2

A series of Ni_3S_4–MoS_2 with different Ni contents were synthesized *via* a one-pot hydrothermal method. The ICP-OES measurements provided the contents of Ni in Ni_3S_4–MoS_2, as shown in Table S1.† The XRD patterns of the Ni_3S_4–MoS_2 composite, pure Ni_3S_4 and MoS_2 are shown in Fig. 1a. For the Ni_3S_4 and MoS_2 samples, all of their peaks were well matching with the Ni_3S_4 (JCPDS no. 47-1739) and MoS_2 phases (JCPDS no. 37-1492), respectively. For the XRD pattern of Ni_3S_4–MoS_2, the diffraction peaks at 14.5°, 32.7° and 58.3° corresponded to the (002), (100) and (110) lattice planes of the MoS_2 phase (JCPDS Card no. 37-1492).[26] There are six sharp peaks at 16.2°, 26.6°, 31.3°, 37.9°, 50.0° and 54.7°, which can be indexed to the (111), (220), (311), (400), (511) and (440) planes of Ni_3S_4 (JCPDS no. 47-1739).[27] The XRD diagram implied the hybrid of these two metal sulfides in Ni_3S_4–MoS_2.

The SEM image of Ni_3S_4–MoS_2 identifies that the morphology of the sample is a hierarchical nanosphere composed of nanosheets with a size of about 1 μm and a thickness of about 30 nm (Fig. 1b). By comparison Fig. 1b with c, it is found that the nanosheets of Ni_3S_4–MoS_2 are bigger and thinner than that of MoS_2 (average size is about 0.6 μm and thickness is 40 nm, as shown in Fig. S1†). Besides, the heterostructure Ni_3S_4–MoS_2 has a larger specific surface area (2.7 m^2 g^{-1}) than that of the pure MoS_2 (0.6 m^2 g^{-1}). The information illustrates that the construction of the heterojunction increased the surface area of samples. The HRTEM images provide further details of the microstructure for the heterostructure Ni_3S_4–MoS_2. The lattice spacing of 0.625 nm corresponds to the (002) plane of MoS_2,[28,29] and 0.28 nm corresponds to the (311) plane of Ni_3S_4,[30] indicating that the sample consisted of Ni_3S_4 and MoS_2. The HRTEM image suggests that the (002) plane of MoS_2 and (311) plane of Ni_3S_4 constitute important heterointerfaces in the composite (Fig. 1d). The crystal structure of the Ni_3S_4–MoS_2 composite was further verified by the select area electron diffraction (SAED) (Fig. 1e). It showed that the inner ring was strong and the outer ring pattern correspond to the (002) plane of the MoS_2 crystal and the (311)

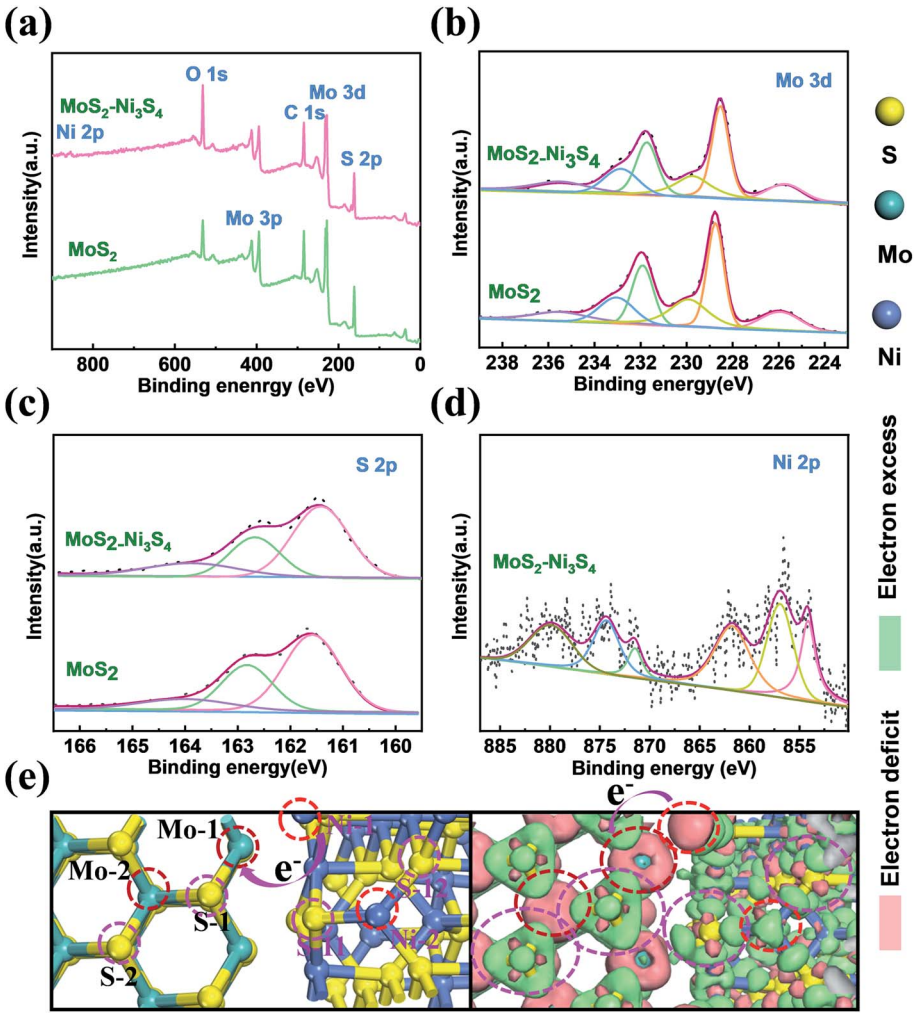

Fig. 2 XPS spectra of Ni_3S_4–MoS_2 and MoS_2: (a) Survey spectra, (b) Mo 3d, (c) S 2p and (d) Ni 2p. (e) Top views of the most stable structure and charge density difference for the Ni_3S_4–MoS_2.

plane of Ni_3S_4, respectively, matching well with the XRD spectra (Fig. 1a). The EDS elemental mapping of Ni_3S_4–MoS_2 indicates that the Mo, S and Ni elements distributed uniformly in the entire nanosheets (Fig. 1f–i), and the contents of Mo, S and Ni of Ni_3S_4–MoS_2 are consistent with the results of ICP-OES tests (Fig. S2 and Table S2†).

XPS spectra were obtained to confirm the chemical composition and valence state of atoms in Ni_3S_4–MoS_2 and pure MoS_2, as shown in Fig. 2. It shows the existence of C, Mo, S, Ni and O elements in Ni_3S_4–MoS_2 and the presence of all the elements but no Ni signal in MoS_2 (Fig. 2a). The O 1s signal was assigned to the absorbed O-containing species, such as O_2, CO_2 and H_2O. The high-resolution Mo 3d spectra of Ni_3S_4–MoS_2 directly evidence the concurrent presence of Mo^{3+} and Mo^{4+} (Fig. 2b) with four definite fitting peaks assigned to Mo^{3+} ($3d_{3/2}$ at 231.8 eV and $3d_{5/2}$ at 228.6 eV) and Mo^{4+} ($3d_{3/2}$ at 232.8 eV and $3d_{5/2}$ at 229.7 eV), respectively.[17] The binding energies of Mo $3d_{5/2}$ and Mo $3d_{3/2}$ in Ni_3S_4–MoS_2 are negative shifts (0.2 eV) compared with the corresponding peaks of pristine MoS_2,[31,32] indicating the lower valence state of Mo in Ni_3S_4–MoS_2. Thus, the charge transfer behavior from Ni_3S_4 to MoS_2 is determined. The change of Mo valence was ascribed to the electronegativity difference between Mo and Ni, where the introduced Ni_3S_4 led to the rearrangement of the electron cloud between Mo and S, thus, forming a new hybridized electronic state. The S 2p spectrum of Ni_3S_4–MoS_2 (Fig. 2c) was deconvoluted into three peaks at 161.4 (S $2p_{3/2}$), 162.6 (S $2p_{1/2}$) and 164.8 eV (S^{2-}), respectively, and the S 2p shifts to the lower binding energy (about 0.2 eV, S $2p_{3/2}$ and S $2p_{3/2}$) compared with the pristine MoS_2 (Fig. 2c), indicating the lower valence state of S in Ni_3S_4–MoS_2. The result was consistent with the previous reports for other transition metals decorated with MoS_2.[33,34] The lower valence state of S in Ni_3S_4–MoS_2 than that in MoS_2 indicated that S in Ni_3S_4–MoS_2 had a higher electric charge density that was contributed to H adsorption, which helped to improve the HER properties. The Ni 2p spectrum of Ni_3S_4–MoS_2, as shown in Fig. 2d, exhibits the apparent Ni $2p_{3/2}$ and $2p_{1/2}$ peaks at 854.8 and 872.1 eV, respectively, that are attributed to Ni^{2+}, and the other peaks at 856.9 and 874.3 eV, attributed to Ni^{3+}.[21] Two satellite peaks at 862.1 and 879.6 eV attributed to Ni $2p_{3/2}$ and $2p_{1/2}$, respectively, were observed.[35] It was further confirmed that the material contained compound Ni_3S_4,[36] which is in agreement with the XRD and HRTEM measurements.

To investigate the electron redistribution on the heterostructure of Ni_3S_4–MoS_2, the electron density different diagram and the Bader charge analysis was performed by DFT calculations (Fig. 2e and Table S3†). The different electron density diagrams demonstrated that the electric charge densities of Mo and S increased on the interfaces Mo-1, S-1 and S-11 in Ni_3S_4–MoS_2, compared with that on the base Mo-2, S-2 and S-12 in Ni_3S_4–MoS_2, indicating that the binding energies of Mo and S in the heterojunction of Ni_3S_4–MoS_2 reduced, which is in accordance with the XPS spectra and Bader charge analysis. The electric charge density of Ni on the interface Ni-1, compared

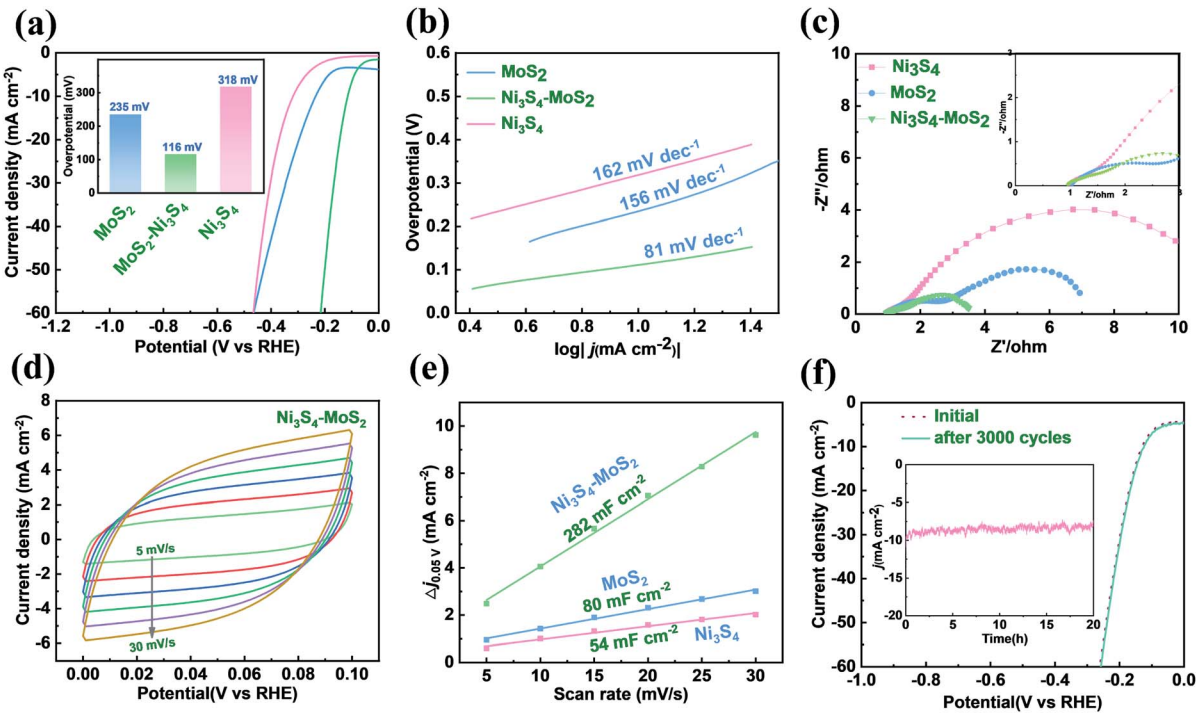

Fig. 3 The HER behavior of Ni_3S_4–MoS_2, Ni_3S_4 and MoS_2 in 1 M KOH. (a) The LSV curves and overpotential (η_{10}) without IR correction. (b) The Tafel slopes. (c) Nyquist plots collected at the overpotential of 180 mV. (d) CV curves of Ni_3S_4–MoS_2 at the scan rates of 5, 10, 15, 20, 25 and 30 mV s^{-1}, respectively. (e) Differences in current density variation ($\Delta J = J_a - J_c$) at 0.05 V *vs.* RHE plotted against scan rate fitted to linear regression for estimation of C_{dl} values of Ni_3S_4–MoS_2, Ni_3S_4 and MoS_2. (f) The initial and 3000th polarization curves of Ni_3S_4–MoS_2. The inset is the chronoamperometric curve recorded at 10 mA for a continuous 20 h.

with that on the base Ni-2 in Ni_3S_4–MoS_2, was decreased, indicating that the electrons were transferred from Ni to Mo or S on the interfaces. These data confirmed the electron redistribution in the heterostructure Ni_3S_4–MoS_2.

HER catalytic behavior

The HER activities of MoS_2, Ni_3S_4–MoS_2 and Ni_3S_4 on NF were measured in a 1 M KOH solution. There was a significant enhancement of the HER activity for Ni_3S_4–MoS_2, as shown in Fig. 3a. The pure MoS_2 exhibited an overpotential of 10 mA cm^{-2} (η_{10}) at 235 mV, which is in agreement with the reported literature.[37] The η_{10} of Ni_3S_4–MoS_2 is 116 mV, which is much lower than that of the pure MoS_2 (235 mV) and pristine Ni_3S_4 (318 mV). The heterostructure Ni_3S_4–MoS_2 showed superior η_{10} in an alkaline solution and is comparable with the electrocatalysts reported in literature (see Table S4† for more details).[38–40] The HER catalytic performance of the electrocatalysts with different Ni contents in Ni_3S_4–MoS_2 was investigated, as shown in Fig. S3,† indicating that Ni_3S_4–MoS_2 with 7.7 wt% Ni has the lowest overpotential (116 mV) at 10 mA cm^{-2} in the alkaline solution.

The Tafel curves of MoS_2, Ni_3S_4–MoS_2 and Ni_3S_4 on NF are shown in Fig. 3b. The Tafel slope of Ni_3S_4–MoS_2 (81 mV dec^{-1}) was much lower than that of MoS_2 (156 mV dec^{-1}), indicating that Ni_3S_4 played a key role in promoting the kinetics of HER. The EIS diagrams exhibited similar impedance characteristics, which implied similar electrochemical processes of these samples (Fig. 3c). Ni_3S_4–MoS_2 showed a much lower charge-transfer-resistance (R_{ct}) value when compared with the other catalysts, suggesting that Ni_3S_4–MoS_2 had better charge-transfer property and HER kinetics. In addition, not only the electric conductivity but also the wettability of MoS_2 was influenced by Ni_3S_4. The contact angle tests of the materials in 1 mol L^{-1} KOH electrolyte were carried out to explain such influence. The contact angle decreased from 21.36° for MoS_2 to 15° for Ni_3S_4–MoS_2 (Fig. S3†). It is shown that Ni_3S_4–MoS_2 had better wettability in the KOH electrolyte than that of initial MoS_2.

Electrochemical active surface area (ECSA) is a standard parameter applied in the evaluation of electrochemical catalysts. To investigate the exposed active sites, the ECSA of Ni_3S_4–MoS_2, MoS_2 and Ni_3S_4 were calculated by the double-layer capacitance (C_{dl}) through plotting CV curves. The CV curves of the samples were tested in the potential range of 0.0–0.1 V at the

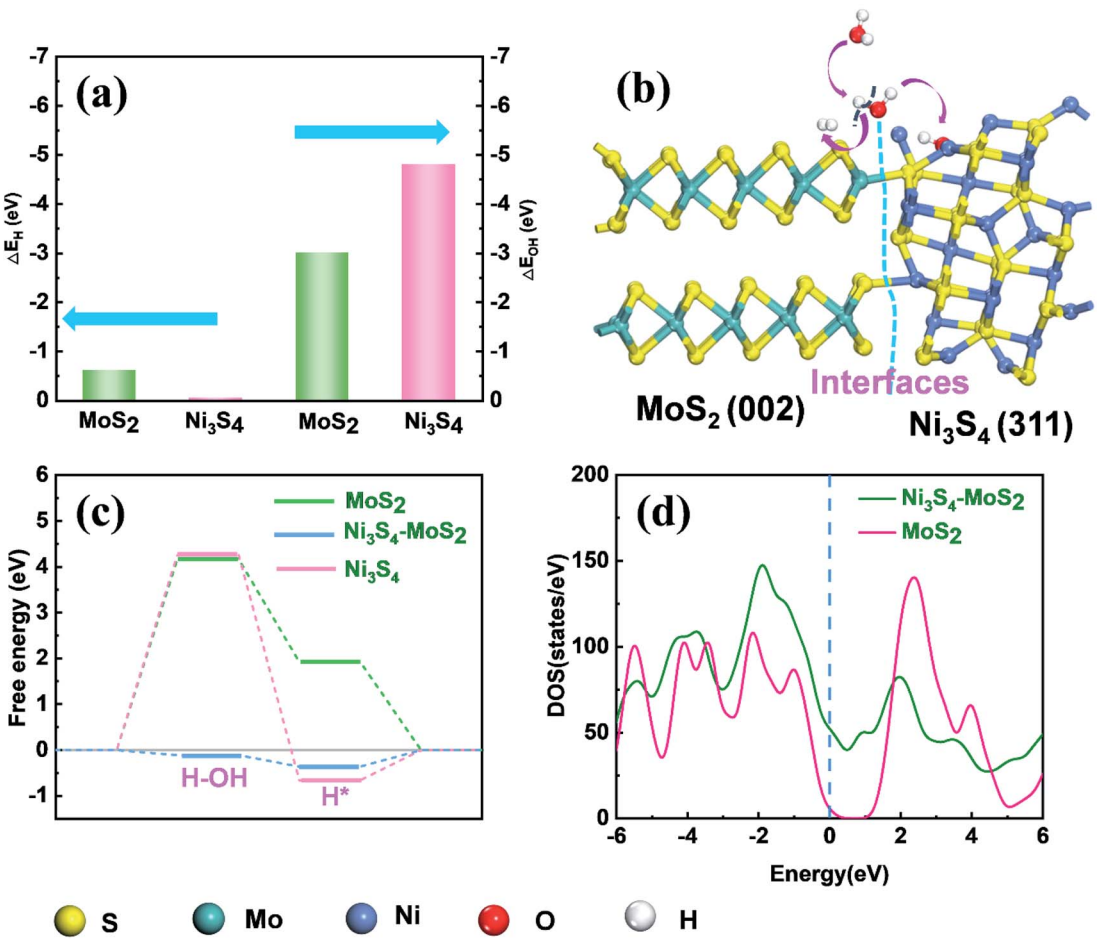

Fig. 4 (a) DFT-calculated adsorption energies of H and OH at different sites on the surfaces of Ni_3S_4–MoS_2, respectively. (b) The illustration of a mechanism for the electrocatalytic HER under alkaline conditions. (c) Free energy diagrams on the surface of MoS_2, Ni_3S_4 and Ni_3S_4–MoS_2 in alkaline solution. (d) DOSs of pristine MoS_2 and Ni_3S_4–MoS_2.

scan rates of 5, 10, 15, 20, 25 and 30 mV s^{-1} in 1.0 M KOH, respectively (Fig. 3d and S5†). The C_{dl} value of Ni_3S_4–MoS_2 was 282 mF cm^{-2}, which is much higher than that of MoS_2 (80 mF cm^{-2}) and Ni_3S_4 (54 mF cm^{-2}) (Fig. 3e), indicating that the additional electrochemical active sites were generated after Ni_3S_4 was introduced. The C_{dl} value of Ni_3S_4–MoS_2 was much more than that of MoS_2 and Ni_3S_4, indicating there are more active sites exposed for HER.

To evaluate the long-term stability of the heterostructure Ni_3S_4–MoS_2, it was subjected to 3000 continuous CV cycles in an alkaline environment from 0 to −0.3 V *vs.* RHE. The LSV curves had no clear changes before and after 3000 CV cycles (Fig. 3f), indicating that Ni_3S_4–MoS_2 has excellent catalytic stability during the electrochemical process. Besides, Ni_3S_4–MoS_2 has a stable HER current at a constant current of 10 mA *versus* time over a 20 h period in 1 M KOH (Fig. 3f). Simultaneously, the morphology of Ni_3S_4–MoS_2 was well preserved (Fig. S6†), demonstrating excellent catalytic stability during the alkaline HER process.

Mechanism of Ni_3S_4–MoS_2 for HER

According to literature,[41,42] DFT calculations were also carried out to gain insight into the underlying mechanism of Ni_3S_4–MoS_2 towards the HER activity. In an alkaline medium, the HER reaction mainly includes three steps: water adsorbed on the catalyst, water dissociation, H* formation and H_2 generation.[43,44] The water dissociation step is considered as the important step for the HER catalytic property in an alkaline solution. The chemisorption free energies of OH (ΔE_{OH}) and H (ΔE_H) on the different sites of Ni_3S_4–MoS_2 were calculated, respectively. To study the optimal chemisorption free energies (ΔE), several feasible positions were chosen for the adsorption of OH and H (Fig. S7†). The chemisorption free energy of H adsorbed on the (002) plane of MoS_2 ($\Delta E_H = -0.81$ eV) was lower than that absorbed on the (311) plane of Ni_3S_4 ($\Delta E_H = -0.027$ eV), indicating that H was inclined to be adsorbed on the (002) plane of MoS_2. Compared with the (002) plane of MoS_2 ($\Delta E_{OH} = -3.0$ eV), the (311) plane of Ni_3S_4 showed a predominant binding energy towards OH ($\Delta E_{OH} = -4.8$ eV), which is attributed to the bonding ability between OH and Ni (Fig. 4a). Therefore, OH is intensely adsorbed on the (311) plane of Ni_3S_4 and H on the (002) plane of MoS_2. The appropriate oxidation of Ni in Ni_3S_4–MoS_2 contributes to the adsorption energy of OH. Simultaneously, the partial reduction of S in Ni_3S_4–MoS_2 is beneficial for the adsorption of H. It demonstrated a synergistic effect of Ni_3S_4–MoS_2 with chemisorption of H (on the (002) plane of MoS_2) and OH (on the (311) plane of Ni_3S_4) accelerated the rate-determining water dissociation steps of HER.

The free energy diagrams on the surfaces of MoS_2, Ni_3S_4 and Ni_3S_4–MoS_2 are shown in Fig. S8.† The ΔG_{H^*} of Ni_3S_4–MoS_2 was −0.36 eV, which was much lower than that of pure MoS_2 (1.92 eV), indicating the superior capacity of Ni_3S_4–MoS_2 for H* adsorption (Table S4†), which benefited from the electron redistribution between Ni_3S_4 and MoS_2. For pure MoS_2, the free energy barrier of water dissociation ΔG_{H_2O} is as high as 4.2 eV, which distinctly hindered the dissociation of H_2O to H*. Moreover, the ΔG_{H2O} of Ni_3S_4–MoS_2 was only −0.10 eV, which was much lower than that of MoS_2 (4.2 eV) and Ni_3S_4 (4.3 eV). It is indicated that the ΔG_{H_2O} of Ni_3S_4–MoS_2 efficiently decreased because of the existence of a heterostructure. Hence, the HER process on Ni_3S_4–MoS_2 is highly accelerated and in accordance with our experimental results.

Moreover, the heterostructure improved the electrical transport efficiency of Ni_3S_4–MoS_2. It is found that the total density of state (DOS) curve of MoS_2 shows a clear band gap at the region around 0 eV, confirming the typical semiconductor characteristic. The peak of the valence band of the heterostructure Ni_3S_4–MoS_2 is close to 0 eV (Fig. 4d), leading to the enhanced excitation of charge carriers to the conduction band and showing better electric conductivity, which is consistent with the EIS tests.

Conclusions

In summary, we fabricated the sphere-shaped heterostructure Ni_3S_4–MoS_2 by a one-pot hydrothermal method. The as-synthesized catalyst with the activated interfaces generated abundant active sites and improved the electrical transport efficiency. Benefiting from engineering the heterostructure, the Ni_3S_4–MoS_2 demonstrated the low overpotential of 116 mV with the corresponding Tafel slope of 81 mV dec^{-1} and long-term stability of over 20 h. DFT calculations proved that the heterostructure Ni_3S_4–MoS_2 resulted in electron redistribution, which indicated the presence of a synergistic effect with MoS_2 as the hydrogen acceptor and Ni_3S_4 as the hydroxyl acceptor, and effectively reduced the intermediate energy barrier of the water dissociation. Hence showing outstanding HER performance in alkaline solution. This work opens the door to develop low-cost and high-activity HER electrocatalyst Ni_3S_4–MoS_2 *via* heterostructure engineering.

Conflicts of interest

The authors declare no competing financial interest.

Acknowledgements

This work was supported by the National Natural Science Foundation of China (nos 2177060378, 21978023, 21627813 and 21521005), the Program for Changjiang Scholars, Innovative Research Teams in Universities (No. IRT1205), and the Fundamental Research Funds for the Central Universities (No. 12060093063 and XK1803-05).

References

1 Z. W. Seh, J. Kibsgaard, C. F. Dickens, I. Chorkendorff, J. K. Norskov and T. F. Jaramillo, Combining theory and experiment in electrocatalysis: Insights into materials design, *Science*, 2017, **355**, eaad4998.
2 M. S. Dresselhaus and I. L. Thomas, Alternative energy technologies, *Nature*, 2001, **414**, 332–337.

3 J. A. Turner, Sustainable hydrogen production, *Science*, 2004, **305**, 972–974.
4 V. R. Stamenkovic, D. Strmcnik, P. P. Lopes and N. M. Markovic, Energy and fuels from electrochemical interfaces, *Nat. Mater.*, 2017, **16**, 57–69.
5 Y. Zheng, Y. Jiao, A. Vasileff and S.-Z. Qiao, The Hydrogen Evolution Reaction in Alkaline Solution: From Theory, Single Crystal Models, to Practical Electrocatalysts, *Angew. Chem., Int. Ed.*, 2018, **57**, 7568–7579.
6 M. Zeng and Y. Li, Recent advances in heterogeneous electrocatalysts for the hydrogen evolution reaction, *J. Mater. Chem. A*, 2015, **3**, 14942–14962.
7 Y. Xu and B. Zhang, Recent advances in porous Pt-based nanostructures: synthesis and electrochemical applications, *Chem. Soc. Rev.*, 2014, **43**, 2439–2450.
8 H. Zhang, P. An, W. Zhou, B. Y. Guan, P. Zhang, J. Dong and X. W. D. Lou, Dynamic traction of lattice-confined platinum atoms into mesoporous carbon matrix for hydrogen evolution reaction, *Sci. Adv.*, 2018, **4**, eaao6657.
9 J. K. Norskov and C. H. Christensen, Chemistry - Toward efficient hydrogen production at surfaces, *Science*, 2006, **312**, 1322–1323.
10 X. Zhang, Z. Lai, C. Tan and H. Zhang, Solution-Processed Two-Dimensional MoS2 Nanosheets: Preparation, Hybridization, and Applications, *Angew. Chem., Int. Ed.*, 2016, **55**, 8816–8838.
11 S. Shi, Z. Sun and Y. H. Hu, Synthesis, stabilization and applications of 2-dimensional 1T metallic MoS2, *J. Mater. Chem. A*, 2018, **6**, 23932–23977.
12 B. Hinnemann, P. G. Moses, J. Bonde, K. P. Jorgensen, J. H. Nielsen, S. Horch, I. Chorkendorff and J. K. Norskov, Biomimetic hydrogen evolution: MoS_2 nanoparticles as catalyst for hydrogen evolution, *J. Am. Chem. Soc.*, 2005, **127**, 5308–5309.
13 T. F. Jaramillo, K. P. Jorgensen, J. Bonde, J. H. Nielsen, S. Horch and I. Chorkendorff, Identification of active edge sites for electrochemical H-2 evolution from MoS_2 nanocatalysts, *Science*, 2007, **317**, 100–102.
14 J. Hu, C. Zhang, L. Jiang, H. Lin, Y. An, D. Zhou, M. K. H. Leung and S. Yang, Nanohybridization of MoS_2 with Layered Double Hydroxides Efficiently Synergizes the Hydrogen Evolution in Alkaline Media, *Joule*, 2017, **1**, 383–393.
15 J. M. Zhang, X. P. Xu, L. Yang, D. J. Cheng and D. P. Cao, Single-Atom Ru Doping Induced Phase Transition of MoS_2 and S Vacancy for Hydrogen Evolution Reaction, *Small Methods*, 2019, **3**, 1900653.
16 Y. Huang, Y. Sun, X. Zheng, T. Aoki, B. Pattengale, J. Huang, X. He, W. Bian, S. Younan, N. Williams, J. Hu, J. Ge, N. Pu, X. Yan, X. Pan, L. Zhang, Y. Wei and J. Gu, Atomically engineering activation sites onto metallic 1T-MoS_2 catalysts for enhanced electrochemical hydrogen evolution, *Nat. Commun.*, 2019, **10**, 982.
17 Y. Wang, F. Lu, K. Su, N. Zhang, Y. Zhang, M. Wang and X. Wang, Engineering Mo-O-C interface in MoS_2@rGO via charge transfer boosts hydrogen evolution, *Chem. Eng. J.*, 2020, **399**, 126018.
18 Y. Liu, S. Jiang, S. Li, L. Zhou, Z. Li, J. Li and M. Shao, Interface engineering of (Ni, Fe)S_2@MoS_2 heterostructures for synergetic electrochemical water splitting, *Appl. Catal., B*, 2019, **247**, 107–114.
19 Y. Li, Z. Yin, M. Cui, X. Liu, J. Xiong, S. Chen and T. Ma, Interface engineering of transitional metal sulfide–MoS_2 heterostructure composites as effective electrocatalysts for water-splitting, *J. Mater. Chem. A*, 2021, **9**, 2070–2092.
20 M. Gong, D. Y. Wang, C. C. Chen, B. J. Hwang and H. J. Dai, A mini review on nickel-based electrocatalysts for alkaline hydrogen evolution reaction, *Nano Res.*, 2016, **9**, 28–46.
21 J. Bao, Y. Zhou, Y. Zhang, X. Sheng, Y. Wang, S. Liang, C. Guo, W. Yang, T. Zhuang and Y. Hu, Engineering water splitting sites in three-dimensional flower-like Co–Ni–P/MoS_2 heterostructural hybrid spheres for accelerating electrocatalytic oxygen and hydrogen evolution, *J. Mater. Chem. A*, 2020, **8**, 22181–22190.
22 J. Cao, J. Zhou, Y. Zhang, Y. Wang and X. Liu, Dominating Role of Aligned MoS_2/Ni_3S_2 Nanoarrays Supported on Three-Dimensional Ni Foam with Hydrophilic Interface for Highly Enhanced Hydrogen Evolution Reaction, *ACS Appl. Mater. Interfaces*, 2018, **10**, 1752–1760.
23 X. Wang, L. Li, Z. Wang, L. Tan, Z. Wu, Z. Liu, S. Gai and P. Yang, NiS_2/MoS_2 on carbon cloth as a bifunctional electrocatalyst for overall water splitting, *Electrochim. Acta*, 2019, **326**, 134983.
24 H. Jiang, K. Zhang, W. Li, Z. Cui, S.-A. He, S. Zhao, J. Li, G. He, P. R. Shearing and D. J. L. Brett, MoS_2/NiS core-shell structures for improved electrocatalytic process of hydrogen evolution, *J. Power Sources*, 2020, **472**, 228497.
25 H. Wang, M. Liang, D. Duan, W. Shi, Y. Song and Z. Sun, Rose-like Ni_3S_4 as battery-type electrode for hybrid supercapacitor with excellent charge storage performance, *Chem. Eng. J.*, 2018, **350**, 523–533.
26 C. Li, M. Liu, H. Ding, L. He, E. Wang, B. Wang, S. Fan and K. Liu, A lightly Fe-doped (NiS_2/MoS_2)/carbon nanotube hybrid electrocatalyst film with laser-drilled micropores for stabilized overall water splitting and pH-universal hydrogen evolution reaction, *J. Mater. Chem. A*, 2020, **8**, 17527–17536.
27 Y. Zhang, W. Sun, X. Rui, B. Li, H. T. Tan, G. Guo, S. Madhavi, Y. Zong and Q. Yan, One-Pot Synthesis of Tunable Crystalline Ni_3S_4@Amorphous MoS_2 Core/Shell Nanospheres for High-Performance Supercapacitors, *Small*, 2015, **11**, 3694–3702.
28 J. Deng, H. Li, J. Xiao, Y. Tu, D. Deng, H. Yang, H. Tian, J. Li, P. Ren and X. Bao, Triggering the electrocatalytic hydrogen evolution activity of the inert two-dimensional MoS_2 surface via single-atom metal doping, *Energy Environ. Sci.*, 2015, **8**, 1594–1601.
29 H. B. Zhang, L. Yu, T. Chen, W. Zhou and X. W. Lou, Surface Modulation of Hierarchical MoS_2 Nanosheets by Ni Single Atoms for Enhanced Electrocatalytic Hydrogen Evolution, *Adv. Funct. Mater.*, 2018, **28**, 1807086.
30 X. Hu, T. Li, Y. Tang, Y. Wang, A. Wang, G. Fu, X. Li and Y. Tang, Hydrogel-Derived Honeycomb Ni_3S_4/N, P-C as an

Efficient Oxygen Evolution Catalyst, *Chem. - Eur. J.*, 2019, **25**, 7561–7568.

31 Y. Feng, T. Zhang, J. Zhang, H. Fan, C. He and J. Song, 3D 1T-MoS_2/CoS_2 Heterostructure via Interface Engineering for Ultrafast Hydrogen Evolution Reaction, *Small*, 2020, **16**, 2002850.

32 S. Qin, T. Yao, X. Guo, Q. Chen, D. Liu, Q. Liu, Y. Li, J. Li and D. He, MoS_2/Ni_3S_4 composite nanosheets on interconnected carbon shells as an excellent supercapacitor electrode architecture for long term cycling at high current densities, *Appl. Surf. Sci.*, 2018, **440**, 741–747.

33 Y. Zhao, S. Wei, F. Wang, L. Xu, Y. Liu, J. Lin, K. Pan and H. Pang, Hatted 1T/2H-Phase MoS_2 on Ni_3S_2 Nanorods for Efficient Overall Water Splitting in Alkaline Media, *Chem. - Eur. J.*, 2020, **26**, 2034–2040.

34 A. Muthurasu, G. P. Ojha, M. Lee and H. Y. Kim, Zeolitic imidazolate framework derived Co_3S_4 hybridized MoS_2–Ni_3S_2 heterointerface for electrochemical overall water splitting reactions, *Electrochim. Acta*, 2020, **334**, 135537.

35 Y. Yang, M.-L. Li, J.-N. Lin, M.-Y. Zou, S.-T. Gu, X.-J. Hong, L.-P. Si and Y.-P. Cai, MOF-derived Ni_3S_4 Encapsulated in 3D Conductive Network for High-Performance Supercapacitor, *Inorg. Chem.*, 2020, **59**, 2406–2412.

36 K. Wan, J. Luo, C. Zhou, T. Zhang, J. Arbiol, X. Lu, B.-W. Mao, X. Zhang and J. Fransaer, Hierarchical Porous Ni_3S_4 with Enriched High-Valence Ni Sites as a Robust Electrocatalyst for Efficient Oxygen Evolution Reaction, *Adv. Funct. Mater.*, 2019, **29**, 1900315.

37 J. Kibsgaard, Z. Chen, B. N. Reinecke and T. F. Jaramillo, Engineering the surface structure of MoS_2 to preferentially expose active edge sites for electrocatalysis, *Nat. Mater.*, 2012, **11**, 963–969.

38 X. Hou, A. Mensah, M. Zhao, Y. Cai and Q. Wei, Facile controlled synthesis of monodispersed MoO_3-MoS_2 hybrid nanospheres for efficient hydrogen evolution reaction, *Appl. Surf. Sci.*, 2020, **529**, 147115.

39 P. Kuang, T. Tong, K. Fan and J. Yu, In Situ Fabrication of Ni–Mo Bimetal Sulfide Hybrid as an Efficient Electrocatalyst for Hydrogen Evolution over a Wide pH Range, *ACS Catal.*, 2017, **7**, 6179–6187.

40 Q. Liu, Z. Xue, B. Jia, Q. Liu, K. Liu, Y. Lin, M. Liu, Y. Li and G. Li, Hierarchical Nanorods of MoS_2/MoP Heterojunction for Efficient Electrocatalytic Hydrogen Evolution Reaction, *Small*, 2020, **16**, 2002482.

41 F. Lin, Z. Dong, Y. Yao, L. Yang, F. Fang and L. Jiao, Electrocatalytic Hydrogen Evolution of Ultrathin Co-Mo_5N_6 Heterojunction with Interfacial Electron Redistribution, *Adv. Energy Mater.*, 2020, **10**, 2002176.

42 J. Hu, J. Liu, Z. Chen, X. Ma, Y. Liu, S. Wang, Z. Liu and C. Huang, Insights into the mechanism of the enhanced visible-light photocatalytic activity of a MoS_2/BiOI heterostructure with interfacial coupling, *Phys. Chem. Chem. Phys.*, 2020, **22**, 22349–22356.

43 C. Hu, L. Zhang and J. Gong, Recent progress made in the mechanism comprehension and design of electrocatalysts for alkaline water splitting, *Energy Environ. Sci.*, 2019, **12**, 2620–2645.

44 C. Zhu, S. Fu, Q. Shi, D. Du and Y. Lin, Single-Atom Electrocatalysts, *Angew. Chem., Int. Ed.*, 2017, **56**, 13944–13960.